lubricants

MDPI

Article

Study of Effect of Nickel Content on Tribocorrosion Behaviour of Nickel–Aluminium–Bronzes (NABs)

C. Berlanga-Labari [1,*], A. Claver [1], M. V. Biezma-Moraleda [2] and José F. Palacio [3]

[1] Engineering Department, Institute for Advanced Materials and Mathematics (INAMAT[2]), Public University of Navarre, Campus Arrosadía s/n, 31006 Pamplona, Spain
[2] Departamento de Ciencia e Ingeniería del Terreno y de los Materiales, Universidad de Cantabria, 39004 Santander, Spain
[3] Centre of Advanced Surface Engineering, AIN, Cordovilla, 31191 Pamplona, Spain
* Correspondence: carlos.berlanga@unavarra.es

Abstract: The simultaneous existence of mechanical erosion and electrochemical corrosion is a common scenario for engineering alloys used in marine environments, such as pump impellers and valves. Nickel–aluminium–bronzes (NABs) are widely used alloys in these environments due to their combination of high corrosion resistance and effective mechanical properties. However, NAB alloys are increasingly cast with reduced nickel content due to its high price and low availability. In this study, we examined the tribocorrosion behaviour of two nickel–aluminium bronzes (C95500 and C95400) with different nickel contents (4.8% and 1.0%, respectively) by means of a pin-on-disk device combined with in situ electrochemistry under 1 M NaCl solution. We conducted tests for pure wear in distilled water, pure corrosion using in situ electrochemistry under 1 M NaCl solution, and a combination of wear and corrosion, called tribocorrosion, to understand the overall synergism that exists between the two. We analysed our results using gravimetric as well as volumetric analysis; in addition, we defined the friction coefficient to compare the effect of open-circuit potential (OCP). We also applied the Tafel method and compared corrosion rates for the different scenarios. We employed confocal microscopy to delimitate the impact of the surface topography of pure wear and its synergistic effect with corrosion, and used an optical microscope to study the materials' microstructures as cast conditions. We also utilised XRD in the Bragg–Brentano configuration to determine the chemical composition of corrosion products. From the experiments conducted, we concluded that an important synergistic effect existed between the wear and corrosion of both NABs, which was associated with corrosion-induced wear. We found NAB C95400 to be more susceptible to erosion under both conditions compared with NAB C95500 due to the chemical composition and lubricant effect of corrosion products formed during the tribocorrosion tests, which were supported by the enriched Ni corrosion products, particularly the presence of nickel-rich copper chloride, $3Cu_3(CuNi)(OH)_6CuCl_2$, in the C95500 alloy. We concluded that, because it increased the nickel content, the NAB alloy offered better wear and corrosion behaviour in sea water conditions due to its protective film nature.

Keywords: corrosion; wear; tribocorrosion; nickel–aluminium–bronze (NAB); kappa phases; lubricant effect; marine environment

Citation: Berlanga-Labari, C.; Claver, A.; Biezma-Moraleda, M.V.; Palacio, J.F. Study of Effect of Nickel Content on Tribocorrosion Behaviour of Nickel–Aluminium–Bronzes (NABs). *Lubricants* **2023**, *11*, 43. https://doi.org/10.3390/lubricants11020043

Received: 27 December 2022
Revised: 18 January 2023
Accepted: 20 January 2023
Published: 28 January 2023

1. Introduction

The term tribology describes the branch of science and technology that studies interacting surfaces in relative motion, which includes the study of friction, wear, lubrication, and cavitation. Tribocorrosion involves the tribological interactions between the mechanically induced interactions with electrochemical processes, causing the materials to corrode at substantially higher rates than those experienced under static or quiescent conditions, enhancing wear processes due to corrosion [1]. Numerous studies on the tribocorrosion behaviour of metallic materials related to biomedical applications, such as Co-Cr and

titanium alloy, have been published over the last 20 years [2–9]. In Jiang et al.'s [10] tribocorrosion modelling proposal for marine alloys, the microstructure, presence of multiple wear mechanisms, localised corrosion, and complex film formation are the key factors to understand this phenomenon, as confirmed by Landolt [11] regarding the role of the passive layer. Huttunen-Saarivirta et al. [12] studied the effect of the absence and presence of tribological contact to determine the tribological behaviour of a leaded tin bronze, concluding that the material losses increased considerably with increases in potential, mainly due to the contribution by wear-induced corrosion to the total material losses. Recently, the tribocorrosion behaviour of a Cu–Ni–Zn alloy in a deep-sea environment was analysed by an in situ electrochemical method, showing that the hydrostatic pressure and electrochemical conditions influence wear morphology and tribocorrosion volume; in addition, the tribocorrosion phenomenon changes from adhesive to abrasive and delamination wear with increasing pressure [13]. Thus, it is necessary to pay attention to all industrial activities wherein tribocorrosion could appear as a phenomenon that decreases the service life of components. Nickel–aluminium–bronze (NAB) alloys are used in the manufacture of different components for marine propulsion systems, such as ship propellers, thrusters, etc., and are also widely used for many internal seawater handling systems as heat-exchanger manifolds, valves, and pipework fittings due to their superior mechanical properties and complex microstructures, which have been attributed for their good corrosion resistance properties. Although there are numerous studies on the corrosion behaviour of NAB in marine environments [14–19], there has been little attention paid to the combined effects of friction and corrosion on this alloy. Basumatary et al. reported that NAB alloys are susceptible to a selective phase attack of the α-κ phase interfaces in the microstructure in corrosive environments [20]; furthermore, Song et al. also showed severe phase corrosion [21]. Song et al. [21] and Schüsller et al. [19] showed that corrosion-inducing ions, which are present in seawater, such as chlorides and sulphates, promote the destruction of the passivation film, leading to high corrosion rates [22]. The properties of NAB are also affected by the appearance of porous copper sulphide in the corrosion film (Song et al. [21] and Schüsller et al. [19]).

Zhang et al. [23] found that NAB alloys' loss of material and friction coefficient during tribocorrosion tests increased with applied load (50–150 N), with the loss primarily attributed to pure mechanical and corrosion-induced wear. In a study carried out in high-pH seawater (10.2), they also found that NAB alloys' susceptibility and corrosion rate increased, resulting in accelerated corrosion-induced wear [24]. Furthermore, they also studied the effect of chloride concentration [25] on the tribocorrosion behaviour of NAB C95800 alloy, concluding that increasing the chloride concentration increased the corrosivity; in addition, it had a good lubricating effect because it alleviated the surface deterioration. Zhang et al. [26] also observed that the relative contribution of corrosion–wear synergism to the total mass loss was greater in 3.5% NaCl solution than in seawater for NAB alloys after tests using a pin-on-disc tribometer integrated to an electrochemical workstation. Corrosion potential is a key factor that can determine whether there is a low or high synergistic effect. In this regard, Huttunen-Saarivirta [27] highlighted that increasing the corrosion potential with respect to the open-circuit potential (OCP) considerably increased the wear caused by the synergistic effect of NAB alloy's corrosion and friction. Recently, Li et al. [28] used NAB to compare the tribological behaviours of Cu-based metal–glass materials (BMG) by sliding in a 3.5 wt% NaCl solution, observing that Cu-based BMG offers better static-corrosion resistance but worse tribocorrosion resistance compared with conventional NAB.

The most significative tribocorrosion studies regarding NAB are linked to the effects of electrolytes, electrochemical conditions, and load, while little attention has been paid to the influence of the percentage of NAB's critical chemical alloy elements on this synergistic phenomenon. Yang et al. [29] found that the influence of nickel content (4.5–10%) balanced the pure corrosion behaviour. They pointed out that increasing the nickel content improved the corrosion resistance due to the incorporation of nickel atoms in the formation of the passive layer; however, the effect of nickel content on the tribocorrosion behaviour of NAB has not yet been analysed. Our work aims to compare the tribocorrosion behaviour of two NAB alloys (C95500 and C95400) in as-cast condition, with different nickel contents (4.8% and 1.0%, respectively), to assess the role of nickel in tribocorrosion by means of pin-on-disk tests using a force of 40 N in a NaCl (1 M) solution, calculating the total material loss rate (T), mechanical wear rate (W_0), and corrosion rate with and without combined effects.

2. Materials and Methods

2.1. Materials

The nickel–aluminium–bronzes (C95500 and C95400) were supplied by a company in as-cast condition. Table 1 shows nickel content is higher in the C95500 alloy (4.8%) compared with the C95400 alloy (1.0%). We measured density in a precision balance applying the Archimedes method; the values were slightly higher for the C95500 alloy. We characterised both alloys by optical microscopy fitted with an image analysis software.

Table 1. Chemical composition and density of NAB C95400 and C95500 alloys.

	Al	Fe	Ni	Mn	Cu	Density (g/cm^3)
C95500	10.0	4.7	4.8	0.4	Balance	7.55 ± 0.02
C95400	10.1	4.1	1.0	0.8	Balance	7.45 ± 0.02

2.2. Tribocorrosion Test and Wear Determination

We ground samples of both alloys using 180-, 800-, and 1500-grit SiC sandpapers (surface finish Ra = 0.40 µm). We performed pin-on-disk tests in NaCl (1 M) solution using Microtest MT series equipment (Microtest S.A.) with 6 mm alumina balls as counterparts, each of which had a surface maximum roughness of Ra_{max} = 0.050 µm and hardness of around 1650 HV. We carried out tests applying 40 N of load to the ball (Hertzian contact stress of 1.9 GPa in the beginning of the test), with 100 rpm and 8 mm track radius. We repeated tests two times to ensure repeatability. Figure 1 shows the components used to perform the tribocorrosion test.

For the calculation of total material loss rate (T) and the mechanical wear rate (W_0), we evaluated the corresponding wear tracks using a confocal smart microscope (Sensofar), and we measured the volume loss straight from the confocal measurements with Sensoview. We performed this measurement in three different zones of the wear tracks, and then extrapolated the obtained average value for the entire wear track using Equation (1). Then, we calculated the wear coefficient value using the equation described in ASTM G99 [30].

$$\frac{V\ loss\ confocal\ \left(\mathrm{m}^3\right)}{wear\ track\ length\ \left(\mathrm{m}\right)} \times 2 \times \Pi \times \mathrm{r}\left(\mathrm{m}\right) = \mathrm{V\,loss}(\mathrm{m}^3) \quad (1)$$

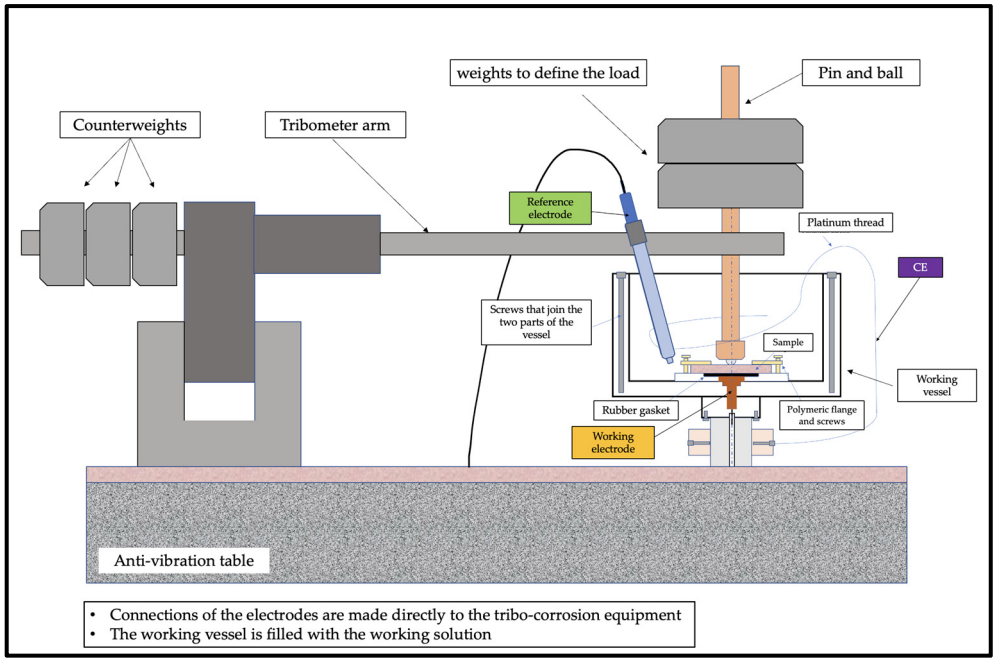

Figure 1. Diagram showing configuration of equipment for tribocorrosion tests.

We performed the assessment of the tribocorrosion behaviour according to the ASTM G119 standard [31], which allowed the quantification of the contributions of wear and corrosion and their synergism to the material degradation by the calculation of the total material loss, T, which is composed of the contribution from pure mechanical wear (W), active dissolution by pure corrosion (C), and the interaction between the two degradation processes called synergy (S), following

$$T = W_0 + C + S \quad (2)$$

The synergy may be twofold: mechanical wear may influence corrosion (ΔCW) and, conversely, corrosion may contribute to mechanical wear (ΔWC), leading to: S = ΔCW + ΔWC.

The synergy component term, ΔC_W, may be defined as: $\Delta C_W = C_W - C_0$, where C_W represents the electrochemical corrosion rate during the corrosive wear. The other term, ΔW_C, may be calculated by: $\Delta W_C = T - W_C - C_W$, where W_C is the wear volume in the presence of corrosion and W_0 is the wear volume in the absence of corrosion, i.e., pure mechanical wear.

We conducted all electrochemical measurements at room temperature with the help of an Autolab potentiostat instrument with a conventional three-electrode system (Figure 1).

First, we carried out open-circuit potential (OCP) measurements for 60 min to achieve stabilization, after which we performed potentiodynamic measurements, sweeping from −500 mV OCP to 500 mV vs. OCP at a rate of 0.5 mV s^{-1}. Thus, the anodic and cathodic polarisation stage had a duration of 16 min. We measured total mass loss (T) and mechanical wear (W_0) values directly from the weight difference prior to and after the test. In addition, to evaluate these two parameters, we employed the wear coefficient from the volume loss, as well as wear track length (Figure 2). To determine the static and dynamic corrosion rate, we carried out the analysis by using the Tafel extrapolation method to obtain the corrosion rate; furthermore, we calculated the penetration rate by applying Faraday's law (Figure 2).

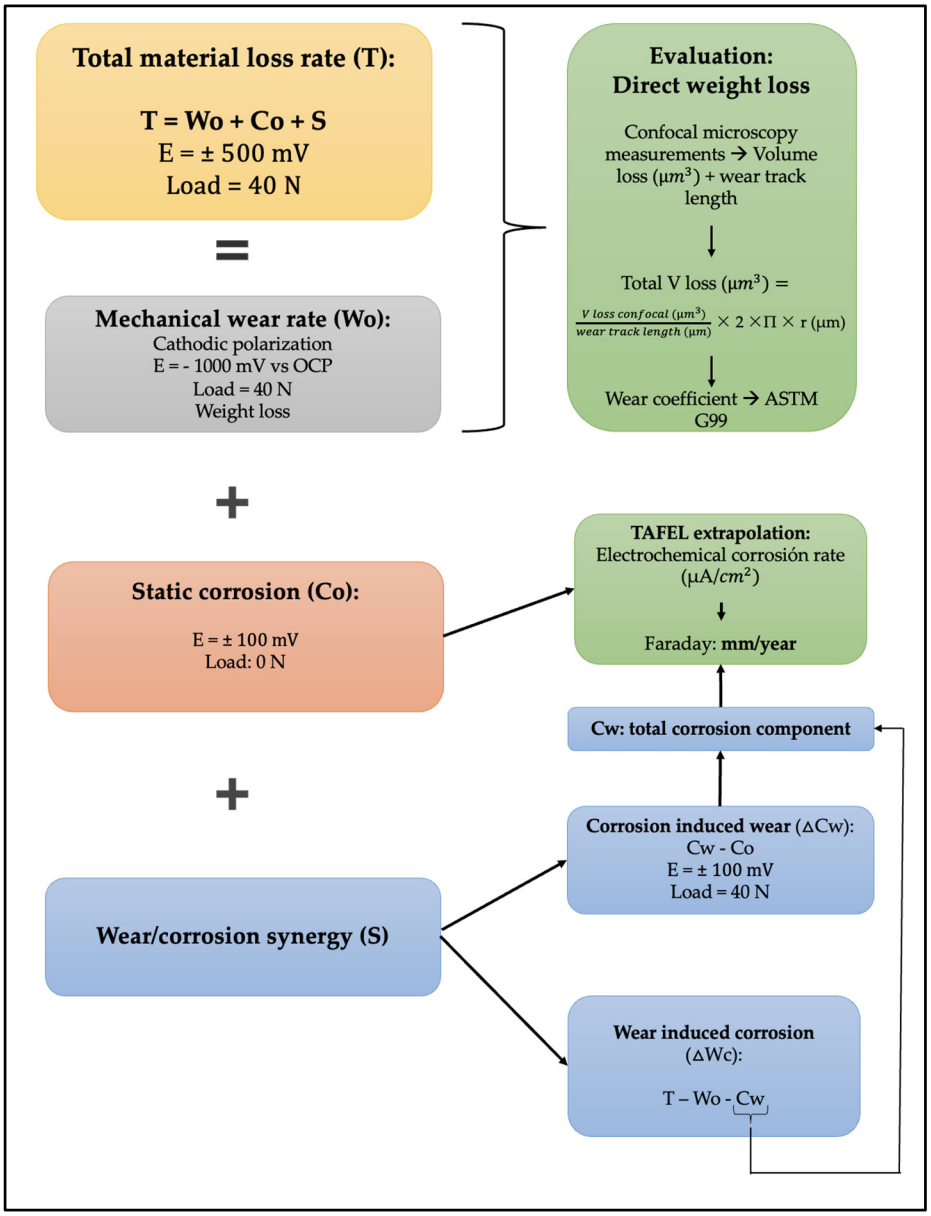

Figure 2. Flow chart showing experimentation performed in this research.

We obtained corrosion products by scraping the surface of the tribocorrosion samples with the help of a stainless steel spatula. The C95400 alloy produced enough sample to carry out an XRD experiment in Bragg–Brentano configuration between 10° to 120° and 0.02° and 5 s per step, using a chromium source with a wavelength of 0.22897 nm. However, the C95400 alloy, did not produce that much of the corrosion product, so the time per step had to be increased to 20 s while keeping the other parameters the same to obtain enough signal and to be able to identify the peaks.

3. Results and Analysis

3.1. Microstructure and Microhardness Characterization

Figure 3 shows that both alloys are composed of the main phases: α, β, and intermetallic compounds called kappa.

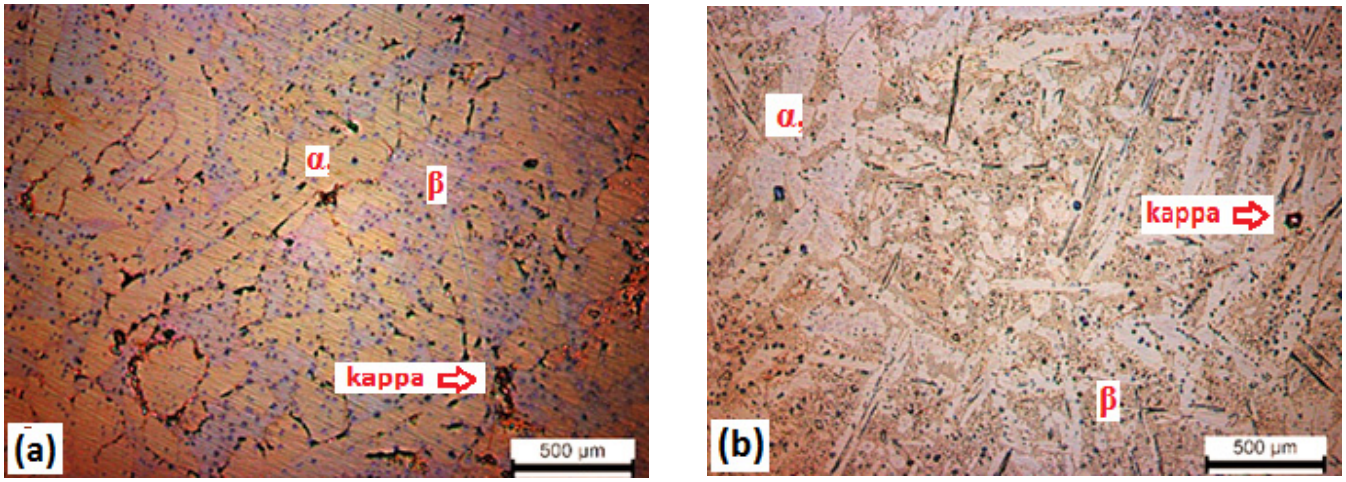

Figure 3. Images obtained from optical microscopy for (**a**) C95500 and (**b**) C95400.

The higher nickel content leads to a higher amount of α phases and intermetallic compounds in the C95500 alloy compared with the C95400 alloy (Table 2). The microhardness of the C95500 alloy is also slightly higher than that of C95400, which is related to the higher intermetallic compounds content.

Table 2. Microstructural image analysis quantification of C95500 and C95400 alloys.

	Alpha Phase (%)	Beta Phase (%)	Intermetallic Compounds (%)	Microhardness ($HV_{0.1}$)
C95500	70.5	24.4	5.1	160 ± 8.2
C95400	53.8	43.0	3.2	145 ± 6.2

3.2. Tribocorrosion Test

We performed combined corrosion and wear tests to obtain information about the tribocorrosion behaviour of the samples. We also carried out potentiodynamic polarization tests in combination with pin-on-disk tests (Figure 2). To do so, first, we monitored the open-circuit potential (OCP) to achieve a stable value. Then, we applied potentiodynamic polarization to the samples. Finally, we monitored OCP again.

The values of the friction coefficients (COFs) over time (Figure 4) are higher for the C95500 alloy (0.4 ± 0.1) compared with the C95400 alloy (0.3 ± 0.1). This fact is associated with the higher hardness (HV = 160 ± 8.2) of the C95500 alloy compared with C95400 (HV = 145 ± 6.2). The evolution is similar in both alloys. We observed a slight initial increase in the cathodic zone, which progressively decreased. The anodic zone showed a relatively stable, low COF value, which is associated with the development of a layer of corrosion products on the metal surface. On the other hand, we observed the variation in the OCP value without polarization (Figure 5). In the same way, as in the previous case, we first recorded the OCP to ensure a stable value; after, we performed the pin-on-disk test. Finally, we again recorded the OCP value without rubbing to show the stabilization of its value.

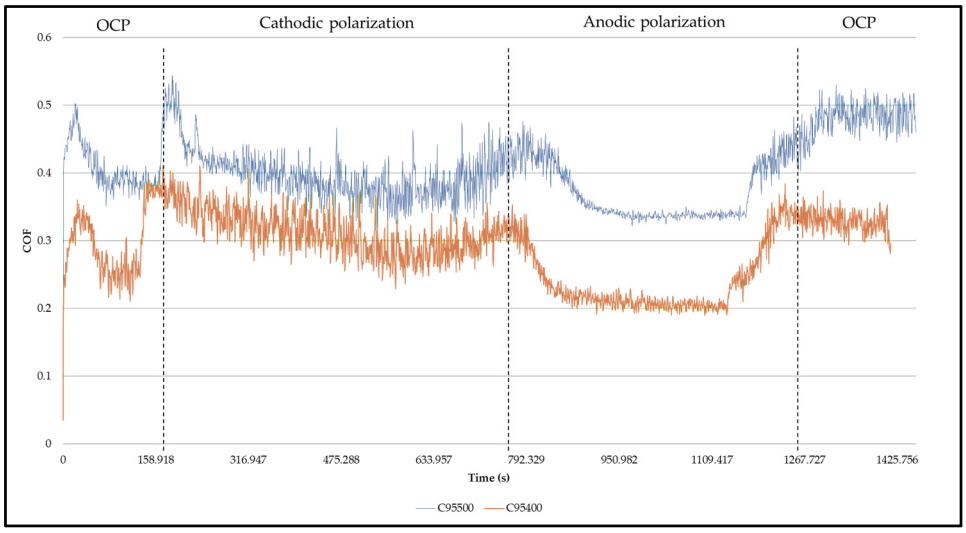

Figure 4. Evolution of coefficient of friction (COF) values with time for C95400 and C95500 alloys.

Both alloys show a similar trend. First, there is a first stabilization stage; then, we observed COF fluctuations during cathodic polarization because no corrosion products formed on the surface samples. After, in the anodic polarization zone, we observed a decrease in COF for both samples, which could be linked to oxides formation. After the anodic polarization step, the coefficient of friction (COF) undergoes a considerable increase to values close to 0.5 for the C95500 alloy and 0.3 for the C95500 alloy. This increase may be associated with the fact that after anodic polarization no new corrosion products are formed; therefore, these products' lubricating effects no longer remain.

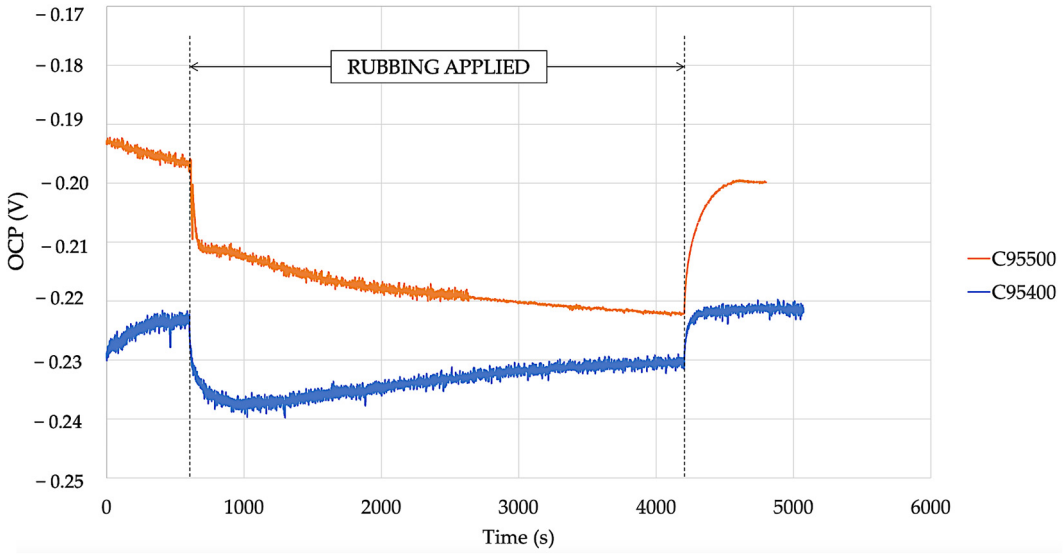

Figure 5. Evolution of OCP values with time for C95400 and C95500 alloys.

Figure 5 shows the evolution of the OCP value over time while the samples are subjected to sliding contact without polarization. The OCP values before wear are slightly higher (E = −0.20 mV) for the C95500 alloy compared with C95400 (E = −0.24 mV). When sliding starts, the decrease in the OCP value is very low, which indicates that a stable passive layer has not been formed as it occurs in the stainless steels. We observed opposite trends in the OCP value's evolution with time during the load application. The OCP value of alloy C95500 shows a trend towards more cathodic potentials. Although this trend was not as significant as that found by Tan et al. [32,33], it suggested that the formation of

corrosion–friction products has some inhibitory effect on the oxygen-reduction reaction. In contrast, the C95400 alloy shows an evolution towards more positive potentials, which are associated with different corrosion–friction products. When the load is removed, the potentials return to the initial values.

3.3. Synergic Study of Corrosion and Friction

Figure 6 shows the results of the static corrosion and tribocorrosion tests. A plateau is evident in the cathodic zone, which is associated with the reduction reactions of dissolved oxygen. No formation of corrosion products has been noted during this period. During anodic polarization, we found no passive layer formation, with a constant increase in the current density that is accelerated by the load effect.

We identified a linear relationship between current density and potential in the proximity of the corrosion potential. We measured the anodic and cathodic slopes and obtained the current densities for the static corrosion and tribocorrosion tests by the Tafel extrapolation method. The corrosion rates obtained from the Tafel analysis showed remarkable differences between static and dynamic corrosion behaviour. When the conditions are static, the corrosion rates are low for both alloys (C_0 = 0.02 mmy^{-1} for alloy B95400 and C_0 = 0.08 mmy^{-1} for alloy B95500). However, when the conditions are corrosive–friction, the corrosion rate significantly increases (C_0 = 1.05 mmy^{-1} for alloy B95400 and C_0 = 1.05 mmy^{-1} for alloy B95500).

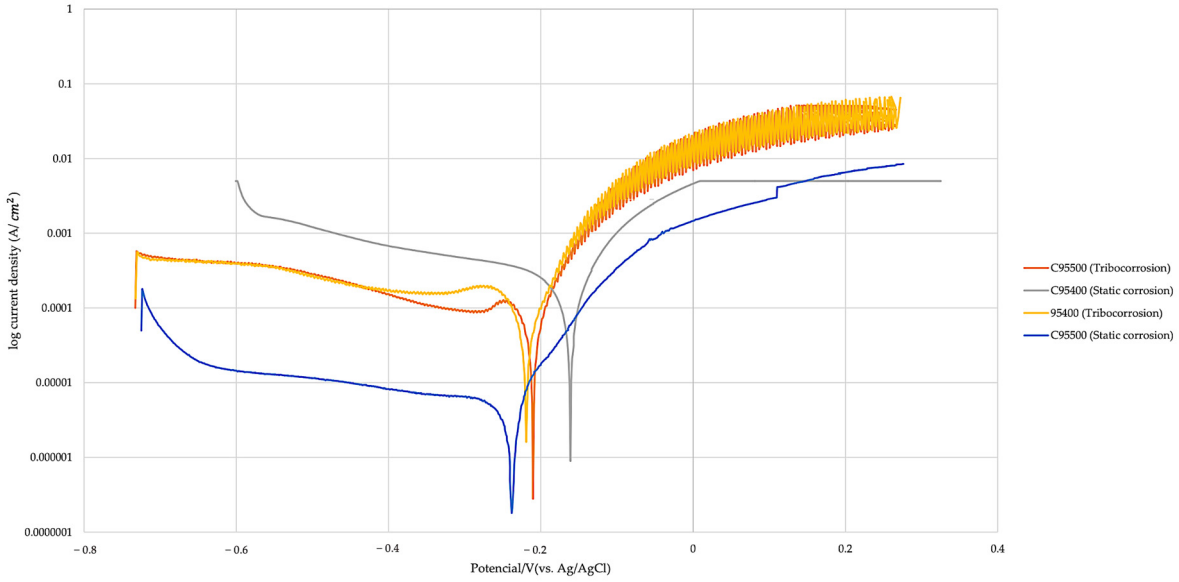

Figure 6. Polarization curves of static corrosion and tribocorrosion of C95400 and C95400 alloys.

Table 3 summarizes that the values for pure mechanical wear (W_0) and static corrosion loss are low (C0). Consequently, most of the total loss (T) is due to the synergy between corrosion and friction (S). The major contribution is corrosion-induced wear for both alloys. (ΔWc). These measurements agree with those obtained by Zhang et al. and Huttunnen ([14,17]) for similar alloys.

Table 3. Summary of various material loss components for C95500 and C95400 alloys.

	T ($mm.y^{-1}$)	W_0 ($mm.y^{-1}$)	Co ($mm.y^{-1}$)	Cw ($mm.y^{-1}$)	S	ΔCw ($mm.y^{-1}$)	ΔWc ($mm.y^{-1}$)
C95500	**143**	**0.08**	**0.02**	**1.05**	**142.9**	1.0	**141.9**
C95400	**163**	**0.13**	**0.05**	**1.35**	**162.8**	1.4	**161.4**

While these alloys do not form stable passive layers under anodic polarization, the corrosion products that are formed help to protect the alloys and prevent an excessive corrosion rate. However, the loading effect tends to remove the corrosion products; therefore, corrosion is not slowed down.

3.4. Wear Evaluation

Figure 7 shows some 3D representations of the wear tracks obtained by confocal microscopy for both materials after rubbing in cathodic polarization (Figure 7a,c) and in tribocorrosion conditions (Figure 7b,d). When we performed wear tests in NaCl solution with cathodic polarization effect, both materials presented longitudinal scratches along the wear track, which are related to pure abrasive wear effect. On the other hand, wear tracks obtained after tribocorrosion tests presented smoother surfaces, which may be due to corrosion products developed in situ during the tests because of their nature.

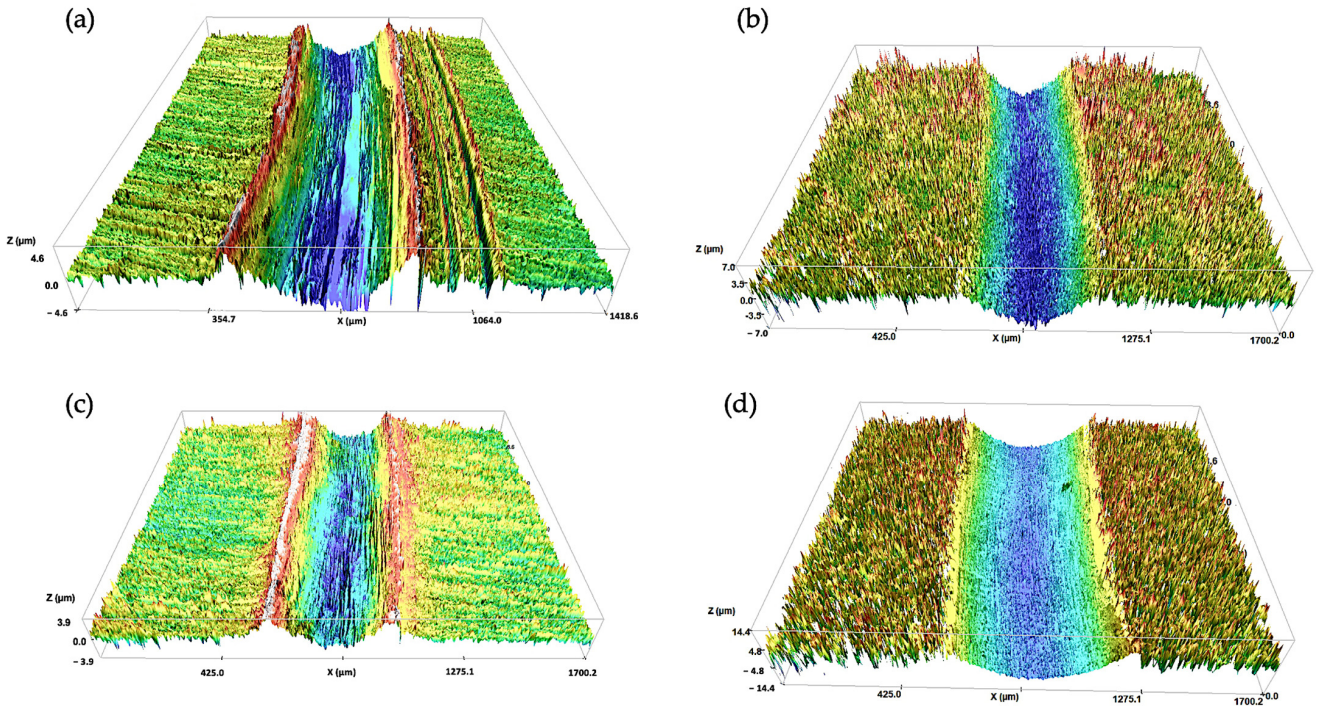

Figure 7. Three-dimensional images of wear tracks obtained by confocal for (**a**) C95500 rubbing in cathodic polarization, (**b**) C95500 in tribocorrosion conditions, (**c**) C95400 rubbing in cathodic polarization, and (**d**) C95400 in tribocorrosion conditions.

Figure 8 shows that the wear track size after the mechanical wear test is small for both alloys, with a maximum depth of 6.5 µm and 6.9 µm for alloys C95400 and C95500, respectively, which considerably increased for both alloys after the tribocorrosion test. For the C95500 alloy, we measured a maximum depth of 51 µm, while for C95400, it was 76 µm. Therefore, the synergistic effect is more remarkable for NAB C95400 than for NAB C95500. In both cases, wear track dimensions and volume loss due to the combined effect of corrosion and wear (T) are considerably higher than the pure mechanical wear (W_0) (Figure 9). The higher volume of material loss in the combined wear and corrosion test with respect to pure mechanical wear tests is reflected in a higher wear rate. The differences are also greater for C95400, as the wear rate increases from 2.9×10^{-6} (mm^3/Nm) to 1.40×10^{-5} (mm^3/Nm), while the value for C95500 merely increases from 3.0×10^{-6} (mm^3/Nm) to 7.0×10^{-6} (mm^3/Nm). These values are consistent with the measurements on the wear track.

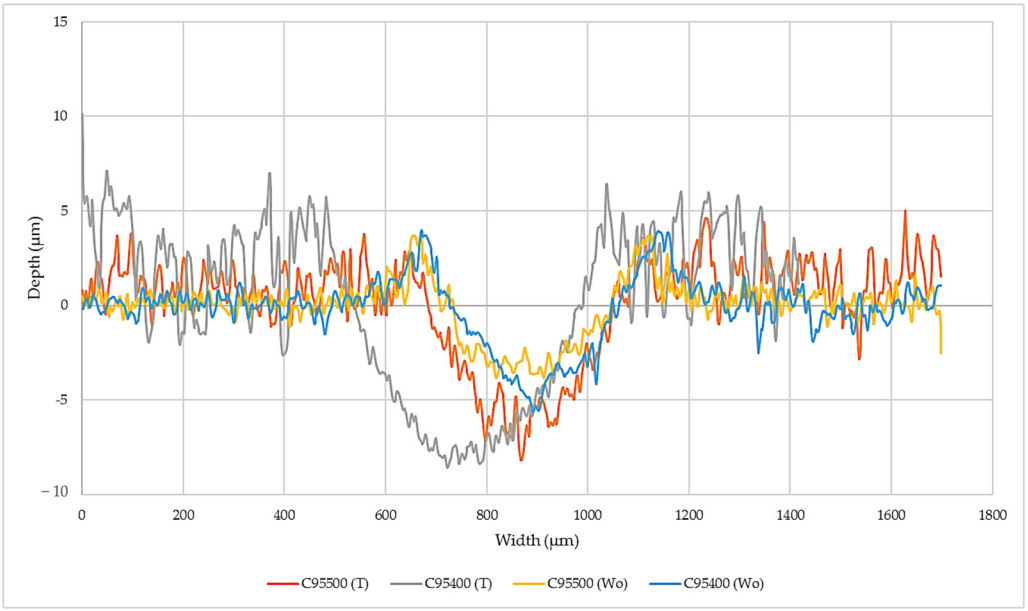

Figure 8. Examples of wear track profiles of mechanical wear (W_0) and tribocorrosion (T) of C95400 and C95500 alloys.

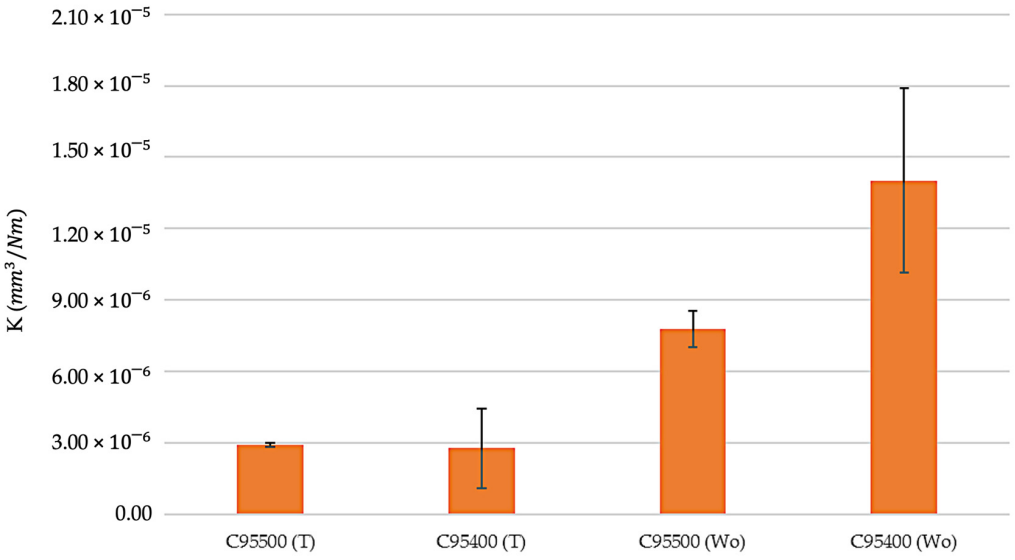

Figure 9. Wear coefficient values of C95400 and C95500 alloys.

3.5. Corrosion–Friction Products Characterization by XRD

Figure 10 shows a diffractogram of corrosion products after the tribocorrosion test.

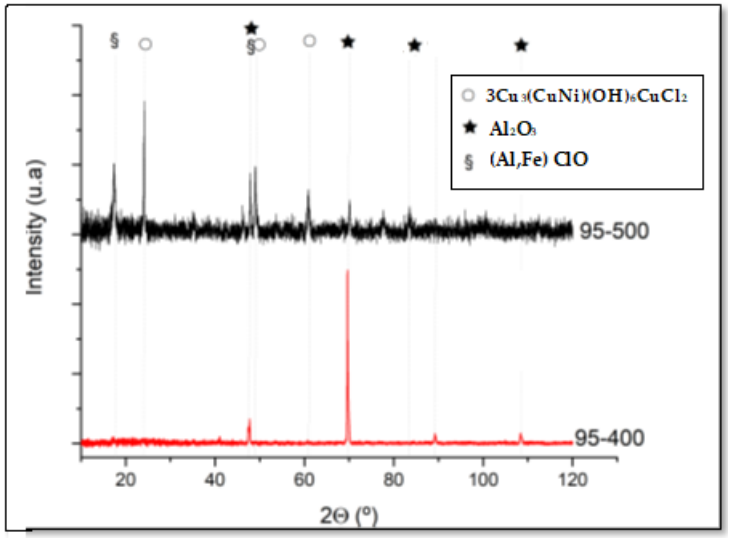

Figure 10. Diffractogram of friction-corrosion products of C95400 and C95500 alloys.

Mainly, aluminium oxide (Al_2O_3) and an oxyhydrochloride of iron and aluminium (Al,Fe) ClO formed in both alloys during the tests; nevertheless, a major compound of nickel-rich copper chloride, $3Cu_3(CuNi)(OH)_6CuCl_2$, was only observed in the C95500 alloy.

4. Conclusions

We performed a novel study on the influence of nickel content on the tribocorrosion behaviour of NAB C95500 and C95400 in 1 M NaCl. We observed a synergistic effect between corrosion and wear in both alloys, mainly due to wear-induced corrosion.

The higher nickel content in the C95500 alloy (Ni: 4.8%) led to better wear-induced corrosion behaviour than the C95400 alloy (Ni: 1.0%). These findings are associated with the formation of corrosion–friction products of a different nature, mainly due to the formation of nickel oxyhydroxides in the C95500 alloy, which causes slightly more desirable tribocorrosion behaviour compared with the C95400 alloy.

More research is needed to better understand the role of microstructures (especially the nature and morphology of kappa intermetallic compounds) in the tribocorrosion behaviour of NABs.

Author Contributions: Conceptualization, C.B.-L.; methodology, C.B.-L., A.C. and M.V.B.-M.; investigation, C.B.-L., A.C., M.V.B.-M. and J.F.P.; writing—original draft preparation, C.B.-L., A.C., M.V.B.-M. and J.F.P.; writing—review and editing, C.B.-L., A.C., M.V.B.-M. and J.F.P.; funding acquisition, C.B.-L., A.C. and M.V.B.-M. All authors have read and agreed to the published version of the manuscript.

Funding: This research was funded by the Gobierno de Cantabria, Spain, grant number: "Estudio del comportamiento frente a cavitacion corrosion de diferentes aleaciones base cobre empleadas en el sector naval, Cavicorrnaval: SUBVTC-2021-0024".

Data Availability Statement: Not applicable.

Acknowledgments: We want to acknowledge Wisco for supplying us with the NAB alloys, as well as the Gobierno de Cantabria, Spain, for funding this research.

Conflicts of Interest: The authors declare no conflict of interest.

References

1. Wood, R.J.K. Marine wear and tribocorrosion. *Wear* **2017**, *376–377*, 893–910. [CrossRef]
2. Alves, A.C.; Oliveira, F.; Wenger, F.; Ponthiaux, P.; Celis, J.-P.; Rocha, L.A. Tribocorrosion behaviour of anodic treated titanium surfaces intended for dental implants. *J. Phys. D Appl. Phys.* **2013**, *46*, 404001. [CrossRef]
3. Correa, D.; Kuroda, P.; Grandini, C.; Rocha, L.; Oliveira, F.; Alves, A.; Toptan, F. Tribocorrosion behavior of β-type Ti-15Zr-based alloys. *Mater. Lett.* **2016**, *179*, 118–121. [CrossRef]
4. Hacisalihoglu, I.; Samancioglu, A.; Yildiz, F.; Purcek, G.; Alsaran, A. Tribocorrosion properties of different type titanium alloys in simulated body fluid. *Wear* **2015**, *332–333*, 679–686. [CrossRef]
5. Sadiq, K.; Black, R.A.; Stack, M.M. Bio-tribocorrosion mechanisms in orthopaedic devices: Mapping the micro-abrasion-corrosion behaviour of a simulated CoCrMo hip replacement in calf serum solution. *Wear* **2014**, *316*, 58–69. [CrossRef]
6. da Silva, F.L.; Antonini, L.M.; Vega, M.R.O.; Aguzzoli, C.; de Fraga Malfatti, C. A New Ternary Alloy Ti26Zr24Nb for Biomedical Application: Behavior in Corrosion, Wear, and Tribocorrosion. *J. Bio-Tribo-Corrosion* **2020**, *6*. [CrossRef]
7. Radice, S.; Neto, M.Q.; Fischer, A.; Wimmer, M.A. Nickel-free high-nitrogen austenitic steel outperforms CoCrMo Alloy regarding tribocorrosion in simulated inflammatory synovial fluids. *J. Orthop. Res.* **2022**, *40*, 1397–1408. [CrossRef]
8. Mace, A.; Gilbert, J.L. Micro-asperity tribocorrosion of CoCrMo, Ti6Al4V, and 316 stainless steel in air and physiological solution: Small scale reciprocal sliding of a single diamond tip. *Wear* **2022**, *498–499*. [CrossRef]
9. Zhang, J.-Q.; Cao, S.; Liu, Y.; Bao, M.-M.; Ren, J.; Li, S.-Y.; Zhang, E.-L.; Wang, J.-J. Tribocorrosion behavior of antibacterial Ti–Cu sintered alloys in simulated biological environments. *Rare Met.* **2022**, *41*, 1921–1932. [CrossRef]
10. Jiang, J.; Stack, M.; Neville, A. Modelling the tribo-corrosion interaction in aqueous sliding conditions. *Tribol. Int.* **2022**, *35*, 669–679. [CrossRef]
11. Landolt, D. Electrochemical and materials aspects of tribocorrosion systems. *J. Phys. D Appl. Phys.* **2006**, *39*, 3121. [CrossRef]
12. Huttunen-Saarivirta, E.; Isotahdon, E.; Metsäjoki, J.; Salminen, T.; Ronkainen, H.; Carpén, L. Behaviour of leaded tin bronze in simulated seawater in the absence and presence of tribological contact with alumina counterbody: Corrosion, wear and tribocorrosion. *Tribol. Int.* **2019**, *129*, 257–271. [CrossRef]
13. Ren, P.; Meng, H.; Xia, Q.; Cui, A.; Zhu, Z.; He, M. Study on the tribocorrosion behavior of Cu–Ni–Zn alloy in deep-sea environment by in-situ electrochemical method. *Wear* **2023**, *514–515*, 204594. [CrossRef]
14. Wharton, J.A.; Barik, R.C.; Kear, G.; Wood, R.J.K.; Stokes, K.R.; Walsh, F.C. The corrosion of nickel-aluminium bronze in seawater. *Corros. Sci.* **2005**, *47*, 3336–3367. [CrossRef]
15. Wu, Z.; Cheng, Y.F.; Liu, L.; Lv, W.; Hu, W. Effect of heat treatment on microstructure evolution and erosion-corrosion behavior of a nickel-aluminum bronze Alloy in chloride solution. *Corros. Sci.* **2015**, *98*, 260–270. [CrossRef]
16. Krogstad, H.N.; Johnsen, R. Corrosion properties of nickel-aluminium bronze in natural seawater—Effect of galvanic coupling to UNS S31603. *Corros. Sci.* **2017**, *121*, 43–56. [CrossRef]
17. Bohm, J.; Linhardt, P.; Strobl, S.; Haubner, R.; Biezma, M. Microstructure of a heat treated nickel-aluminum bronze and its corrosion behavior in simulated fresh and sea water. *Mater. Perform. Charact.* **2016**, *5*, 689–700. [CrossRef]
18. Linhardt, P.; Kührer, S.; Ball, G.; Biezma, M.V. Design of a multichannel potentiostat and its application to corrosion testing of a nickel-aluminum bronze. *Mater. Corros.* **2017**, *69*, 358–364. [CrossRef]
19. Schüssler, A.; Exner, H.E. The corrosion of nickel-aluminium bronzes in seawater-I. Protective layer formation and the passivation mechanism. *Corros. Sci.* **1993**, *34*, 1793–1802. [CrossRef]
20. Basumatary, J.; Wood, R. Different methods of measuring synergy between cavitation erosion and corrosion for nickel aluminium bronze in 3.5% NaCl solution. *Tribol. Int.* **2020**, *147*, 104843. [CrossRef]
21. Song, Q. Investigation on the Corrosion and Cavitation Erosion Behaviors of the Cast and Friction Stir Processed Ni-Al Bronze in Sulfide-Containing Chloride Solution. *Int. J. Electrochem. Sci.* **2017**, *12*, 10616–10632. [CrossRef]
22. Ma, J.; Hou, G.; Cao, H.; An, Y.; Zhou, H.; Chen, J.; Duan, W. Why does seawater corrosion significantly inhibit the cavitation erosion damage of nickel-aluminum bronze? *Corros. Sci.* **2022**, *209*, 110700. [CrossRef]
23. Zhang, B.; Wang, J.; Yan, F. Load-dependent tribocorrosion behaviour of nickel-aluminium bronze in artificial seawater. *Corros. Sci.* **2018**, *131*, 252–263. [CrossRef]
24. Zhang, B.-B.; Wang, J.-Z.; Yuan, J.-Y.; Yan, F.-Y. Tribocorrosion behavior of nickel aluminum bronze in seawater: Identification of corrosion-wear components and effect of Ph. *Mater. Corros.* **2017**, *69*, 106–114. [CrossRef]
25. Zhang, B.; Wang, J.; Yuan, J.; Yan, F. Tribocorrosion behavior of nickel-aluminium bronze sliding against alumina under the lubrication by seawater with different halide concentrations. *Friction* **2019**, *7*, 444–456. [CrossRef]
26. Zhang, B.; Wang, J.; Liu, H.; Yuan, J.; Jiang, P.; Yan, F. Assessing the Tribocorrosion Performance of Nickel–Aluminum Bronze in Different Aqueous Environments. *Tribol. Trans.* **2019**, *62*, 314–323. [CrossRef]
27. Huttunen-Saarivirta, E.; Isotahdon, E.; Metsäjoki, J.; Salminen, T.; Carpén, L.; Ronkainen, H. Tribocorrosion behaviour of aluminium bronze in 3.5 wt.% NaCl solution. *Corros. Sci.* **2018**, *144*, 207–223. [CrossRef]
28. Ji, X.; Zhao, J.; Jin, J.; Wu, J.; Zhu, W. Tribological Behavior of Cu-Based Bulk Metallic Glass Compared to Nickel–Aluminum Bronze in Air and 3.5% Sodium Chloride Solution. *J. Tribol.* **2023**, *145*, 041701. [CrossRef]
29. Yang, F.; Kang, H.; Guo, E.; Li, R.; Chen, Z.; Zeng, Y.; Wang, T. The role of nickel in mechanical performance and corrosion behaviour of nickel-aluminium bronze in 3.5 wt.% NaCl solution. *Corros. Sci.* **2018**, *139*, 333–345. [CrossRef]

30. *ASTM G99–17*; Standard Test Method for Wear Testing with a Pin-on-Disk Apparatus. American Society for Testing and Materials: West Conshohocken, PA, USA, 2017.
31. *ASTM G119*; Standard Guide for Determining Synergism Between Wear and Corrosion. American Society for Testing and Materials: West Conshohocken, PA, USA, 2017.
32. Tan, B.; Lan, S.; Zhang, S.; Deng, H.; Qiang, Y.; Fu, A.; Ran, Y.; Xiong, J.; Marzouki, R.; Li, W. Passiflora edulia Sims leaves Extract as renewable and degradable inhibitor for copper in sulfuric acid solution. *Colloids Surfaces A Physicochem. Eng. Asp.* **2022**, *645*, 128892. [CrossRef]
33. Tan, B.; Lan, S.; Zhang, S.; Deng, H.; Qiang, Y.; Fu, A.; Ran, Y.; Xiong, J.; Marzouki, R.; Li, W. Insight into the anti-corrosion performance of two food flavors as eco-friendly and ultra-high performance inhibitors for copper in sulfuric acid medium. *J. Colloid Interface Sci.* **2022**, *609*, 838–851. [CrossRef] [PubMed]